



# Evolution of strain across the magnetostructural phase transition in epitaxial FeRh films on different substrates

Jon Ander Arregi <sup>1,\*</sup>, Ondřej Caha,<sup>2</sup> and Vojtěch Uhlíř <sup>1,3,†</sup>

<sup>1</sup>CEITEC BUT, Brno University of Technology, Purkyňova 123, 612 00 Brno, Czech Republic

<sup>2</sup>Department of Condensed Matter Physics, Faculty of Science, Masaryk University, Kotlářská 2, 611 37 Brno, Czech Republic

<sup>3</sup>Institute of Physical Engineering, Brno University of Technology, Technická 2, 616 69 Brno, Czech Republic



(Received 15 August 2019; revised manuscript received 8 April 2020; accepted 16 April 2020; published 8 May 2020)

We present a detailed x-ray diffraction study of the structural evolution of epitaxial FeRh films across the temperature-driven phase transition between antiferromagnetic and ferromagnetic order. FeRh films grown onto MgO, W/MgO, and Al<sub>2</sub>O<sub>3</sub> substrates show qualitatively different lattice distortions (tetragonal vs rhombohedral), while keeping a sharp transition above room temperature. Temperature-dependent x-ray reciprocal space mapping reveals the phase-specific crystal structure, giving access to both in-plane and out-of-plane lattice parameters and crystalline coherence lengths across different stages of the phase transition. Diffuse x-ray scattering from relaxed films is treated via a mosaic block model, which provides a robust data fitting scheme. It is found that the ferromagnetic phase fraction can stand a larger amount of strain before completely annihilating and transitioning to the antiferromagnetic phase upon cooling, as compared to heating. This is related to the distinct magnetic exchange correlations in the antiferromagnetic and ferromagnetic parent phases.

DOI: [10.1103/PhysRevB.101.174413](https://doi.org/10.1103/PhysRevB.101.174413)

## I. INTRODUCTION

Materials with interconnected structural and magnetic degrees of freedom often show emergent physical phenomena and multifunctional properties such as prominent magnetoelastic, magnetoresistive, or magnetocaloric effects [1–6]. These phenomena are particularly pronounced in connection with a magnetostructural phase transition [7], which in turn allows controlling the physical properties of the material via several types of externally applied driving forces. A prototypical example for this material class is the equiatomic and chemically ordered FeRh alloy, undergoing a first-order magnetostructural phase transition from antiferromagnetic (AF) to ferromagnetic (FM) order just above room temperature ( $T_M \sim 360$  K) [8,9]. In thin films, the transition typically presents a thermal hysteresis of around 10 K between the cooling and heating cycles. It is accompanied by an isotropic lattice expansion (0.5%) [10] and a reduction in resistivity (50%), as a result of coupled structural, electronic, and magnetic order parameters [11–13]. This feature of FeRh allows control of the phase transition via temperature, magnetic field [14], strain [15,16], electrical currents [17], or ultrafast optical pulses [18–22]. The associated changes in magnetization, magnetoresistance, and entropy make FeRh an interesting material for magnetic recording [23], spintronic devices [24], or magnetic refrigeration [25]. Epitaxial FeRh films also constitute a suitable magnetic platform for integration of two-dimensional (2D) materials, such as graphene [26].

While the most stable crystal structure of FeRh in both AF and FM phases corresponds to a cubic CsCl-type lattice [10], epitaxial strain in thin films caused by the mismatch with the substrate leads to lattice distortions. Strain and microstructure have profound consequences on the character of the phase transition; for instance, compressive or tensile strain tends to stabilize the AF or FM phase, respectively [14,27–29]. Transition properties of FeRh thin films have been investigated for a great variety of substrates, such as glass or quartz [30,31], MgO and Al<sub>2</sub>O<sub>3</sub> [14], ion beam assist deposited MgO (IBAD-MgO) [32], W [33,34], Ge [35], KTaO<sub>3</sub> and SrTiO<sub>3</sub> [36], among others. A number of works also aimed at controlling the phase transition using electric fields by coupling the film to a piezoelectric substrate such as BaTiO<sub>3</sub> [15,16,37,38] and PMN-PT [39,40].

Beyond modifications of the transition temperature, the film microstructure and strain also affects the preferential orientation of magnetic moments in FeRh. In particular, tetragonal distortion of FeRh films makes Fe spins adopt in-plane or out-of-plane preferential orientation depending on the lattice parameter ratio  $c/a$ , with a spin reorientation occurring at the phase transition [32]. This phenomenon presents interesting options for utilizing FeRh in spintronic devices where AF magnetoresistance effects could be exploited [24]. Therefore, obtaining a good understanding of the lattice distortions across the phase transition in FeRh is crucial for the assessment and control of its magnetic behavior.

A number of works have characterized the evolution of FeRh lattice parameter across the AF-to-FM phase transition using x-ray or neutron diffraction. These works, however, only focused on bulklike specimens [10,41] or films deposited onto MgO, where the evolution of the out-of-plane lattice

\*ja.arregi@ceitec.vutbr.cz

†vojtech.uhlir@ceitec.vutbr.cz

parameter alone was reported [42–44]. In the same way, description of the crystal structure across the phase transition for FeRh systems on different substrates with significantly different lattice distortions has not been reported thus far.<sup>1</sup>

In this work, we study the thermally induced magnetostructural transition in FeRh films on different substrates via x-ray diffraction (XRD). We have analyzed epitaxial FeRh films grown on different substrate systems: MgO(001), W(001)/MgO(001), and Al<sub>2</sub>O<sub>3</sub>(0001). These substrates provide different growth conditions (dielectric vs metal) and exert a distinct deformation (compressive vs tensile, tetragonal vs rhombohedral) in FeRh films, which are critical parameters having impact on the phase transition. For thin films the abrupt first-order transition broadens and a pronounced phase coexistence appears due to different parts of the sample possessing slightly different transition temperatures [45,46]. By measuring temperature-dependent reciprocal space maps, we resolve the evolution of the AF- and FM-phase-specific lattice distortions during the transition, where coexistence of the two phases occurs. Analysis using a mosaic-block model of the diffuse x-ray scattering reveals fine structural details, giving access to out-of-plane and in-plane lattice parameters as well as vertical and lateral correlation lengths of the crystalline lattice. Furthermore, we have investigated the asymmetric strain features during the heating and cooling cycles, pointing to the different role of exchange interactions in each direction of the transition. Our study unveils the interplay of AF and FM phases in terms of the phase-dependent strain inherent in the system, which contributes to the understanding of the phase transition in FeRh on the meso- and nanoscale [43,47,48].

## II. EXPERIMENTAL METHODS

FeRh films were deposited using magnetron sputtering from an equiatomic FeRh target at a base pressure lower than  $5 \times 10^{-8}$  mbar. Epitaxial FeRh thin films of different thicknesses were grown on MgO(001) and Al<sub>2</sub>O<sub>3</sub>(0001) substrates, with the substrates being preheated to 723 K for 1 h before deposition. Film growth was performed at the same temperature at a fixed Ar pressure ranging between  $2.5 \times 10^{-3}$  and  $2.8 \times 10^{-3}$  mbar. The typical deposition rate for FeRh was around 0.03 nm/s. In case of the FeRh films epitaxially grown onto W buffer layers on MgO, an approximately 10-nm-thick W layer was grown first on MgO(001) substrates at 723 K, following 1 h of substrate preheating. All samples were postgrowth annealed at 1073 K for 30 to 60 min in the same chamber, for the purpose of obtaining the desired CsCl-type (*B2* ordering) crystal structure. A protective 2-nm-thick Pt capping layer was subsequently deposited on all FeRh films once they were cooled down below 373 K.

The temperature-dependent magnetization was measured via vibrating sample magnetometry (VSM) using a Quantum Design VersaLab magnetometer in the temperature range of 200–400 K and in an in-plane applied magnetic field of 1 T.

<sup>1</sup>Additionally, time-resolved transient strain generated across the transition upon ultrafast laser pulse excitation has been reported [20,21]. However, this effect does not describe the equilibrium lattice evolution occurring upon thermal cycling.

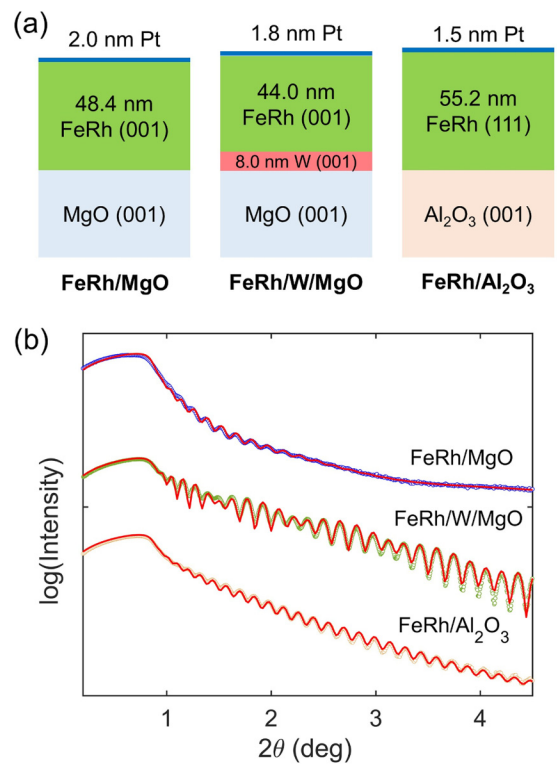


FIG. 1. (a) Configuration of the representative FeRh films employed in the study, indicating the fitted thickness values obtained from the x-ray reflectivity (XRR) data. (b) XRR data (open symbols) and corresponding fits (solid lines) for the FeRh/MgO, FeRh/W/MgO, and FeRh/Al<sub>2</sub>O<sub>3</sub> epitaxial films.

The structural analysis of the samples was performed via x-ray reflectivity (XRR) and XRD using a Rigaku SmartLab (9 kW) diffractometer with Cu *K*α radiation ( $\lambda = 1.5406 \text{ \AA}$ ). A double-bounce Ge(022) monochromator and a 5° Soller slit were employed in the incident and diffractive optics, respectively. For the temperature-dependent XRD measurements, the sample was placed in a high-temperature chamber with a hemispherical dome made of graphite, using a N<sub>2</sub> gas environment for improved temperature homogeneity. Reciprocal space maps were acquired performing coupled  $2\theta/\omega$  scans at different  $\omega$  orientations between the x-ray source and the sample.

## III. RESULTS AND DISCUSSION

### A. Structural and magnetic properties of FeRh films on different substrates

The thickness and layer structure of the FeRh samples has been characterized via XRR (see Fig. 1), which reveals that the films grow smoothly on all MgO(001), Al<sub>2</sub>O<sub>3</sub>(0001), or W(001)/MgO(001) substrates. The XRR profiles were fitted to a multilayer model from which we extracted the measured FeRh thicknesses of 48.4 nm (on MgO), 44.0 nm (on W/MgO), and 55.2 nm (on Al<sub>2</sub>O<sub>3</sub>) [49]. For the FeRh film on W/MgO, we have optimized the FeRh film deposition on top of the W buffer layer such that the magnetostructural phase transition occurs above room temperature. We concluded that the thickness of the W buffer layer should be between 8 and

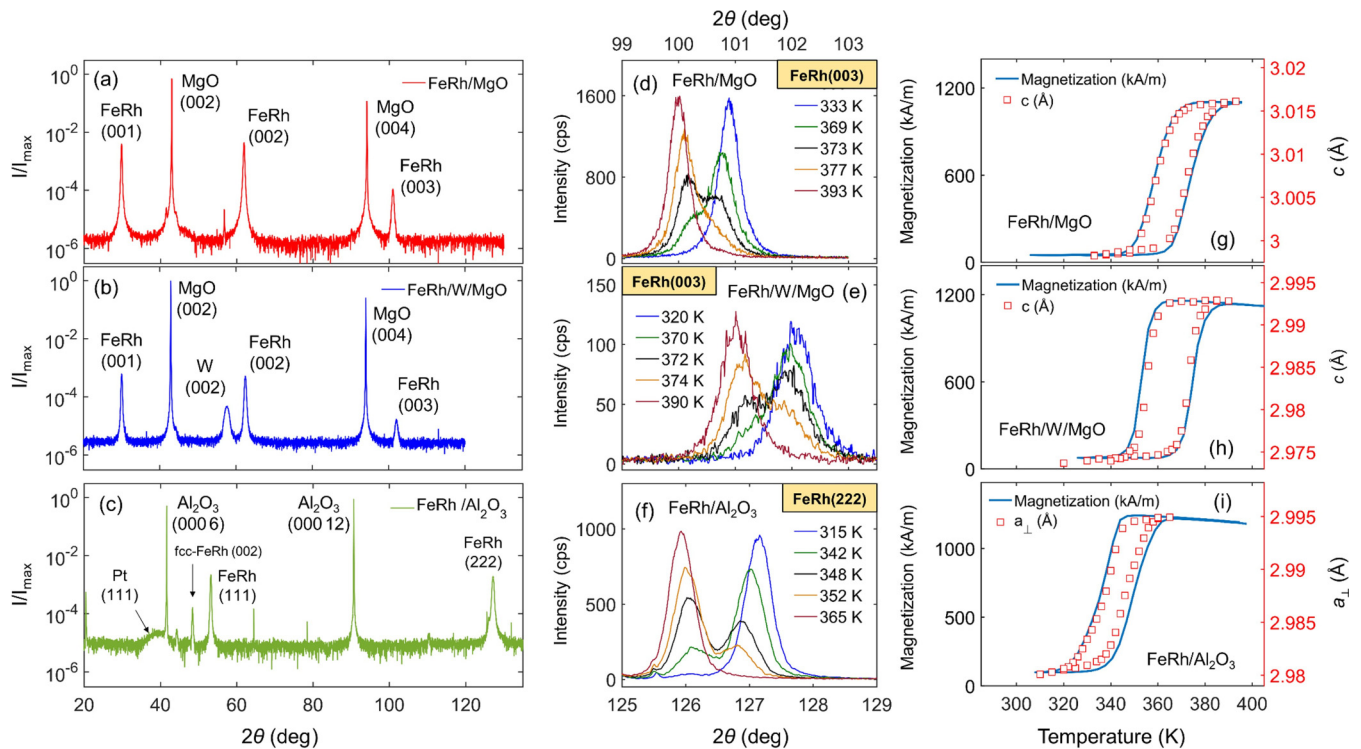


FIG. 2. (a–c) Room temperature XRD  $\theta$ - $2\theta$  scans for the FeRh/MgO, FeRh/W/MgO, and FeRh/Al<sub>2</sub>O<sub>3</sub> films. (d–f) Temperature-dependent  $\theta$ - $2\theta$  scans during heating around the FeRh(003) diffraction peak for the films on MgO and W/MgO or around the FeRh(222) for the film on Al<sub>2</sub>O<sub>3</sub>. (g–i) Superimposed temperature-dependent magnetization (left) and average out-of-plane lattice parameter (right) data for the same samples. The magnetization data were corrected for the effect of applied magnetic field.

10 nm (being 8.0 nm for the sample in Fig. 1). The FeRh/W interface has a fitted roughness value below 0.5 nm, indicating negligible intermixing of the metallic layers despite the 1-h-long postgrowth annealing employed here [49]. This suggests that the W/MgO system is a highly appropriate template for the growth of metamagnetic FeRh. The XRR measurements confirm Pt capping layer thicknesses of around 2 nm for all samples, sufficient to avoid oxidation of the FeRh layers.

Symmetric XRD  $\theta$ - $2\theta$  scans at room temperature [Figs. 2(a)–2(c)] indicate a high texture level of the FeRh films on all three substrate systems. FeRh(001) textured films are obtained for both MgO and W/MgO substrates, evidenced by the (00 $l$ ) diffraction peaks present up to the third order in Figs. 2(a) and 2(b). The 8-nm-thick W buffer layer also shows a (001) texture as evidenced by the W(002) peak. The film on Al<sub>2</sub>O<sub>3</sub>(0001) exhibits FeRh(111) texture via the appearance of the (111) and (222) diffraction peaks [Fig. 2(c)]. The x-ray spectra in Fig. 2(c) also exhibit a broad, low-intensity Pt(111) peak arising from the capping layer, as well as an additional peak at  $2\theta = 48.4^\circ$  corresponding to the (002) reflection of fcc FeRh. This residual phase with a crystalline order different from the CsCl type typically appears in slightly Rh-rich FeRh films on  $c$ -plane sapphire, due to the substantial lattice mismatch between FeRh and Al<sub>2</sub>O<sub>3</sub> [50]. Pole figure analysis of FeRh films on Al<sub>2</sub>O<sub>3</sub> substrates did not indicate any preferential in-plane texture for the detected fcc FeRh fraction. Thus, we attribute the appearance of the paramagnetic fcc residuals [51] to the misfit dislocations introduced upon accommodation of the predominant CsCl-type FeRh structure onto Al<sub>2</sub>O<sub>3</sub>(0001).

Figures 2(d) and 2(e) display several selected temperature-dependent  $\theta$ - $2\theta$  scans acquired during heating around the FeRh(003) Bragg peak for films on MgO and W/MgO. A single peak is present at lower temperatures, which corresponds to a well-ordered fully AF phase. As temperature increases, the peak splits into two, indicating coexistence of AF and FM phases [42,43]. The peak at higher (lower)  $2\theta$  values decreases (increases) gradually in intensity upon heating. Finally, a single peak at a lower  $2\theta$  value indicates a larger lattice parameter corresponding to a fully FM phase. Figure 2(f) shows temperature-dependent  $\theta$ - $2\theta$  scans for the FeRh(222) reflection from the film on Al<sub>2</sub>O<sub>3</sub>, where an increase in lattice parameter is also demonstrated upon heating.

The magnetostructural phase transition in FeRh films is followed by extracting the out-of-plane lattice parameter during the heating and cooling cycles. Figures 2(g)–2(i) show the weighted average lattice parameter data for films on MgO, W/MgO, and Al<sub>2</sub>O<sub>3</sub> across the phase transition. The out-of-plane lattice parameter for the film on MgO [in the range of 2.995–3.016 Å, Fig. 2(g)] is always (irrespective of the phase) greater than for the film on W/MgO [2.972–2.995 Å, Fig. 2(h)]. Despite the opposite strain exerted by the two substrates, the transition temperatures during heating and cooling are similar for the FeRh films on MgO and W/MgO. However, in the case of the Al<sub>2</sub>O<sub>3</sub> substrate, the exerted tensile strain apparently shifts the transition towards lower temperatures. The temperature-dependent magnetization [solid lines in Figs. 2(g)–2(i)] shows excellent agreement with the average out-of-plane lattice parameter. The saturation magnetization value of around  $1150 \times 10^3$  A/m at 400 K is in line with

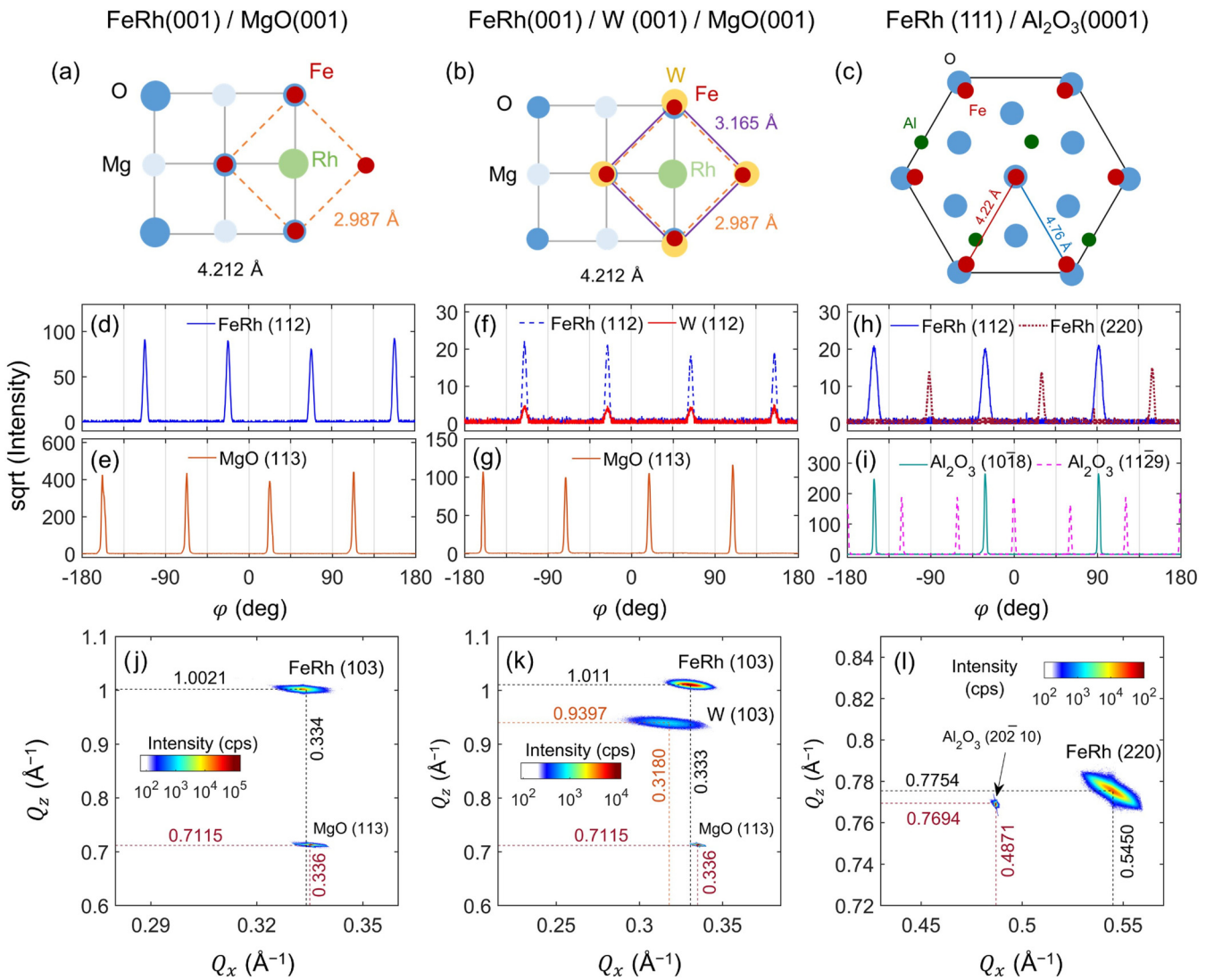


FIG. 3. (a)-(c) Schematics of the film-to-substrate lattice matching in the films considered in this study. The central panel exhibits XRD azimuthal scans ( $\varphi$  scans) evidencing in-plane epitaxial relationships for (d,e) FeRh/MgO, (f,g) FeRh/W/MgO, and (h,i) FeRh/ $\text{Al}_2\text{O}_3$ . X-ray reciprocal space maps showing asymmetric film and substrate diffraction peaks measured along the same azimuthal direction of the sample, which are representative of the intended in-plane epitaxial matching lengths: (j) FeRh(103) and MgO(113); (k) FeRh(103), W(103), and MgO(113); (l) FeRh(220) and  $\text{Al}_2\text{O}_3(20\bar{2}10)$ .

previous studies [14] and a nearly zero magnetization is found for all samples at room temperature. A residual magnetization value of a few percent is generally observed at room temperature, as a result of stoichiometric inhomogeneities, crystalline defects, and ferromagnetically stabilized regions at the film interfaces [52,53].

The strain in FeRh films exerted by the different substrates was further analyzed from the in-plane epitaxy. Figures 3(a)–3(c) show schematics of the epitaxial matching of FeRh and substrate crystals. The cubic FeRh lattice with a bulk lattice parameter of 2.987 Å at room temperature [10] presents excellent epitaxial matching to the fcc cubic lattice of MgO ( $a = 4.212$  Å) with a relative 45° in-plane rotation [Fig. 3(a)]. The MgO substrate induces an in-plane compressive strain resulting from the lattice mismatch of  $\varepsilon_{\text{FeRh-MgO}} = 0.3\%$ . This leads to FeRh film growth with a tetragonal distortion of  $c/a > 1$  [14]. In order to stabilize FeRh films with  $c/a < 1$ ,

growth on IBAD-MgO has been often employed [32]. In our case a thin W buffer layer ( $a = 3.165$  Å) is deposited in between MgO and FeRh [Fig. 3(b)] for this purpose. The high lattice mismatch between W and MgO ( $\varepsilon_{\text{W-MgO}} = 6.3\%$ ) induces a substantial compressive in-plane strain in the W lattice. However, high-quality epitaxial W films on MgO can be achieved over a wide W film thickness range [54]. To some extent, the thickness-dependent strain relaxation can be exploited to lower the in-plane lattice parameter of a thin W film grown onto MgO, which reduces lattice mismatch for FeRh growth. Earlier it has been observed that FeRh films grown on 40-nm-thick W buffer layers on MgO are massively strained ( $c/a < 0.9$ ), which led to suppression of the magnetostructural phase transition [55]. Apparently, considerably thinner W films (8–10 nm) reduce the high mismatch between the bulk W and FeRh lattices ( $\varepsilon_{\text{FeRh-W}} = -5.6\%$ ). This leads to moderate in-plane tensile strain in FeRh while keeping

TABLE I. Lattice parameters of the epitaxial FeRh films grown on MgO, W/MgO, and Al<sub>2</sub>O<sub>3</sub> while in the AF (300 K) and FM (400 K) phase. The quantities in parentheses indicate the strain value with respect to the bulk FeRh lattice parameter at 300 K;  $a = b = c = 2.987 \text{ \AA}$ .

	300 K (AF phase)			400 K (FM phase)		
	$c$ (Å)	$a$ (Å)	$c/a$	$c$ (Å)	$a$ (Å)	$c/a$
FeRh/MgO	$2.9953 \pm 0.0002$ (+0.28%)	$2.9820 \pm 0.0003$ (-0.17%)	$1.0045 \pm 0.0001$	$3.0157 \pm 0.0001$ (+0.96%)	$2.9856 \pm 0.0004$ (-0.05%)	$1.0101 \pm 0.0001$
FeRh/W/MgO	$2.9722 \pm 0.0001$ (-0.50%)	$2.9956 \pm 0.0003$ (+0.29%)	$0.9922 \pm 0.0001$	$2.9948 \pm 0.0001$ (+0.26%)	$2.9981 \pm 0.0005$ (+0.37%)	$0.9989 \pm 0.0002$
	$a_R$ (Å)	$\gamma_R$ (deg.)		$a_R$ (Å)	$\gamma_R$ (deg.)	
FeRh/Al <sub>2</sub> O <sub>3</sub>	$2.9936 \pm 0.0002$ (+0.2%)	$90.26 \pm 0.04$		$3.0050 \pm 0.0003$ (+0.6%)	$90.12 \pm 0.06$	

the desired  $c/a < 1$  tetragonal distortion [49]. Finally, Figure 3(c) represents the epitaxial matching of FeRh(111) films on Al<sub>2</sub>O<sub>3</sub>(0001). In this case, the substrate exerts a substantial in-plane tensile strain as a result of a large lattice mismatch, amounting to  $\varepsilon_{\text{FeRh-Al}_2\text{O}_3} = -11.3\%$ . The distance between Fe (Rh) atoms in the (111) plane and the  $a$ -plane lattice parameter of Al<sub>2</sub>O<sub>3</sub> are 4.224 and 4.759 Å, respectively. Epitaxial growth, however, is still possible at the cost of introducing a large amount of misfit dislocations (as indicated by the presence of a residual fcc-FeRh phase) and a relatively high misorientation of the crystalline grains. The majority CsCl-type FeRh lattice fraction presents a rhombohedral distortion, featuring a compressed unit cell along the out-of-plane [111] direction.<sup>2</sup>

Figures 3(d) and 3(e) display azimuthal XRD scans ( $\varphi$  scans), where the MgO(113) and FeRh(112) diffraction peak intensities are monitored while rotating the sample. The four-fold symmetry and the 45° shift between the film and substrate peaks confirm the alignment of FeRh[100] with MgO[110]. Figures 3(f) and 3(g) show the same measurement for the FeRh film on W/MgO, with the addition of the W(112) buffer layer reflection, corroborating that the [100] directions of FeRh and W match in the film plane. Finally, the  $\varphi$  scans for the (112) and (220) diffraction peaks of FeRh (spaced by 120°) in Fig. 3(h) indicate the threefold in-plane symmetry of the FeRh film on Al<sub>2</sub>O<sub>3</sub>. The azimuthal scans for the (10 $\bar{1}$ 8) and (11 $\bar{2}$ 9) substrate reflections in Fig. 3(i) demonstrate that the FeRh[11 $\bar{2}$ ] lattice direction is aligned with Al<sub>2</sub>O<sub>3</sub>[10 $\bar{1}$ 0] in the sample plane.

<sup>2</sup>Due to the FeRh film growth at 723 K, the lattice mismatch is altered for the high-temperature lattice configuration. The actual mismatch between FeRh and MgO is slightly larger, whereas the growth on both W/MgO and Al<sub>2</sub>O<sub>3</sub> substrates is facilitated given the mismatch decrease at 723 K with respect to room temperature. We assume that additional irreversible changes in terms of dislocations occur upon cooling the film to room temperature after growth. In the main text the room temperature mismatch values are used as a reference. Following [2,10] we estimated the mismatch values at 723 K:  $\varepsilon_{\text{FeRh-MgO}} \sim 0.48\%$ ,  $\varepsilon_{\text{W-MgO}} \sim 5.9\%$ ,  $\varepsilon_{\text{FeRh-W}} \sim -5.1\%$ , and  $\varepsilon_{\text{FeRh-Al}_2\text{O}_3} = -10.8\%$ .

The bottom panel of Fig. 3 exhibits the in-plane matching conditions of the FeRh films in reciprocal space.<sup>3</sup> The film/substrate combined x-ray scans along a given sample azimuth are taken for diffraction peaks belonging to lattice planes oblique to the sample surface. Diffraction peaks possessing nearly equal in-plane components of the reciprocal space vector are considered in each panel. Hence, for perfect epitaxial film-to-substrate matching, one would observe their peaks vertically aligned at the same  $Q_x$  value, indicating commensurate lattices. The overlap in  $Q_x$  indicates how well a film is accommodated to the substrate along the in-plane direction of the sample.

Figure 3(j) displays the FeRh/MgO case, where the FeRh(103) peak is centered at a lower  $Q_x$  value than MgO(113). This means that the in-plane lattice parameter of FeRh is slightly larger than the MgO matching  $a_{\text{MgO}}/\sqrt{2}$  dimension, confirming the in-plane compressive strain exerted by the substrate. A similar data set which additionally includes the W(103) peak is shown in Fig. 3(k) for the FeRh/W/MgO system. From the relative deviation in  $Q_x$  of the MgO(113), W(103), and FeRh(103) reflections, we conclude that the W film is strongly contracted in plane, due to the large mismatch with the MgO lattice underneath. In the same way, the FeRh film is considerably expanded in-plane as compared to the case in Fig. 3(j), due to the tensile strain exerted by W. Even though the FeRh film here also has a larger in-plane lattice parameter than  $a_{\text{MgO}}/\sqrt{2}$ , this difference is now more noticeable than in FeRh/MgO as a result of the W buffer layer. Finally, the reciprocal space maps of in Fig. 3(l) reveal that the FeRh film on Al<sub>2</sub>O<sub>3</sub> has significantly released its tensile strain as deduced from the moderate difference in the  $Q_x$  peak position for FeRh(220) and Al<sub>2</sub>O<sub>3</sub>(20 $\bar{2}$ 10).

The lattice parameters of the fully AF and FM phases have been quantitatively characterized for all samples by measuring reciprocal space maps at 300 and 400 K, respectively [49]. The results are summarized in Table I, where the out-of-plane and in-plane lattice parameters  $c$  and  $a$ , as well as their ratio  $c/a$ , are indicated for FeRh films on MgO and W/MgO. When warming up to 400 K, the main lattice expansion occurs in the out-of-plane direction for both films on MgO

<sup>3</sup>Throughout the paper, we define the reciprocal space axes as  $Q_x = \frac{1}{\lambda}[\cos(2\theta - \omega) - \cos \omega]$  and  $Q_z = \frac{1}{\lambda}[\sin(2\theta - \omega) + \sin \omega]$ .

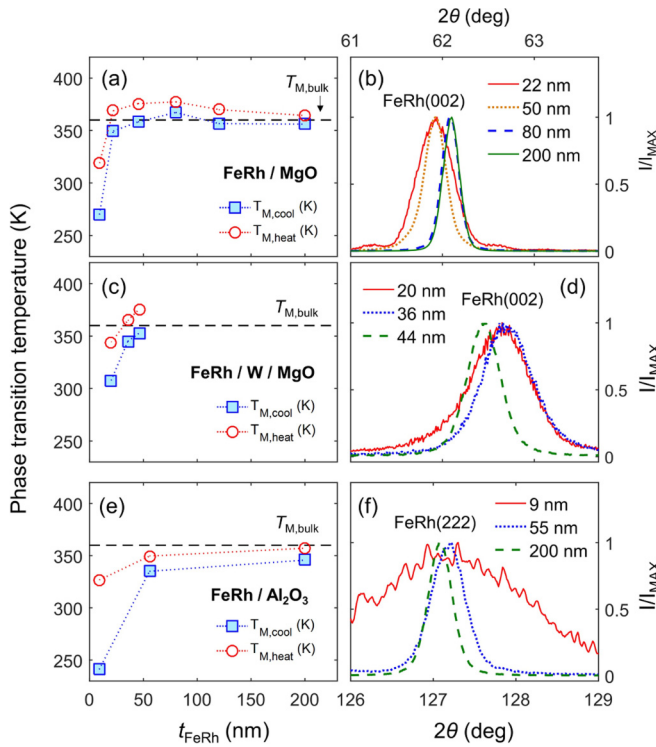


FIG. 4. Left panel: Thickness dependence of the phase transition temperature  $T_M$  during cooling (squares) and heating (circles) for FeRh films on (a) MgO, (c) W/MgO, and (e) Al<sub>2</sub>O<sub>3</sub>, extracted from VSM measurements. The horizontal dashed line represents the phase transition temperature for bulk FeRh ( $\sim 360$  K). The right panel displays room-temperature symmetric x-ray  $\theta$ - $2\theta$  scans for FeRh films with different thicknesses near the FeRh(002) or FeRh(222) reflections for films on (b) MgO, (d) W/MgO, and (f) Al<sub>2</sub>O<sub>3</sub>. Only  $\theta$ - $2\theta$  scans for films in the fully AF phase at room temperature are shown.

and W/MgO. The actual change in  $a$  is about an order of magnitude lower than that in  $c$ . In the case of FeRh/MgO, the tetragonal distortion becomes more prominent at 400 K, while for FeRh/W/MgO, the principal increase in  $c$  compensates the distortion at 300 K by bringing the  $c/a$  value closer to one. For the film on Al<sub>2</sub>O<sub>3</sub>, the rhombohedral lattice can be represented by a single lattice parameter value  $a_R$  and the rhombic angle  $\gamma_R$ . A value of  $\gamma_R$  slightly greater than  $90^\circ$  at 300 K confirms the effective in-plane tensile strain exerted by the Al<sub>2</sub>O<sub>3</sub> substrate on the FeRh film. This strain is partially relaxed when warming up to 400 K, as indicated by the small reduction in  $\gamma_R$ .

### B. Film-thickness-dependent strain and phase transition temperature

The thickness of FeRh films with qualitatively different lattice distortions has a significant impact on the magnetostructural phase transition. The thickness dependence of the transition temperature has been reported for films on MgO, KTaO<sub>3</sub>, and SrTiO<sub>3</sub> [36], but not for films on W/MgO and Al<sub>2</sub>O<sub>3</sub>. Figure 4 exhibits the phase transition temperature during the heating and cooling cycles for films of different thickness grown on MgO, W/MgO and Al<sub>2</sub>O<sub>3</sub>. The case

of FeRh/MgO is depicted in Fig. 4(a), where two different thickness-dependent trends are apparent. For films thicker than 40 nm, an increase in thickness is associated with a slight reduction of the phase transition temperatures  $T_{M,\text{cool}}$  and  $T_{M,\text{heat}}$ . This phenomenon is explained in terms of a thickness-dependent strain relaxation of the FeRh film, such that the transition temperature shows a recovery towards the bulk value ( $T_{M,\text{bulk}} = 360$  K) upon increasing the film thickness. Exemplary  $\theta$ - $2\theta$  scans for the FeRh(002) reflection in FeRh/MgO films [Fig. 4(b)] confirm that with increasing thickness the FeRh(002) peak shifts to the right, indicating strain relief. On the contrary, a reduction in the transition temperature occurs upon reducing the film thickness below  $t_{\text{FeRh}} < 40$  nm, in particular below 20 nm. The stabilization of the FM phase at room temperature and the phase transition temperature reduction in ultrathin FeRh films on MgO has already been studied theoretically and experimentally. Its origin has been attributed to stoichiometry inhomogeneities and increased stress due to the substrate [56,57], as well as to the role of ferromagnetically stabilized film fractions near Rh-terminated interfaces [52,58].

For the W/MgO and Al<sub>2</sub>O<sub>3</sub> substrates [Figs. 4(c) and 4(e)] we observe a single trend in FeRh film thickness. The transition temperature approaches the bulk value at high  $t_{\text{FeRh}}$  values and it monotonically decreases upon reducing the film thickness. In these two cases, the in-plane strain generated by the substrate tends to expand the FeRh lattice, hence stabilizing the FM phase and lowering the transition temperature. Exemplary  $\theta$ - $2\theta$  scans for the films on W/MgO and Al<sub>2</sub>O<sub>3</sub> [Figs. 4(d) and 4(f), respectively] verify that with increasing thickness both FeRh(002) and FeRh(222) peaks shift to the left and become narrower, indicating relaxation of the compressive out-of-plane strain. However, there is no available theoretical prediction of the FM stabilized phase in films on W/MgO and Al<sub>2</sub>O<sub>3</sub>. The steep decrease in the transition temperature for lower thicknesses could be related to strain accumulation as well as to the increasing presence of composition inhomogeneities due to the mismatch with the substrate.

### C. Temperature-dependent evolution of the phase-specific crystal structures

XRD reciprocal space maps across the entire region of the magnetostructural phase transition were measured for FeRh films on the different substrates. These data sets provide detailed information about the FeRh lattice structure in the transition region, where coexistence of AF and FM phases occurs, allowing to investigate their mutual interplay. Reciprocal space maps were obtained for both symmetric and asymmetric diffraction peaks, giving access to structural details in the out-of-plane and in-plane directions. The mathematical representation of diffuse x-ray scattering from relaxed films presenting defects such as misfit or threading dislocations is not simple. We have followed the work by Holý and co-workers in which relaxed layers are mathematically represented in the form of densely packed, randomly rotated mosaic blocks of spheroidal shape [59,60]. Within this model, it is assumed that the crystal lattice of a block is randomly rotated and not strained. The block boundaries are defined by networks of threading dislocations, such that the model is characterized by

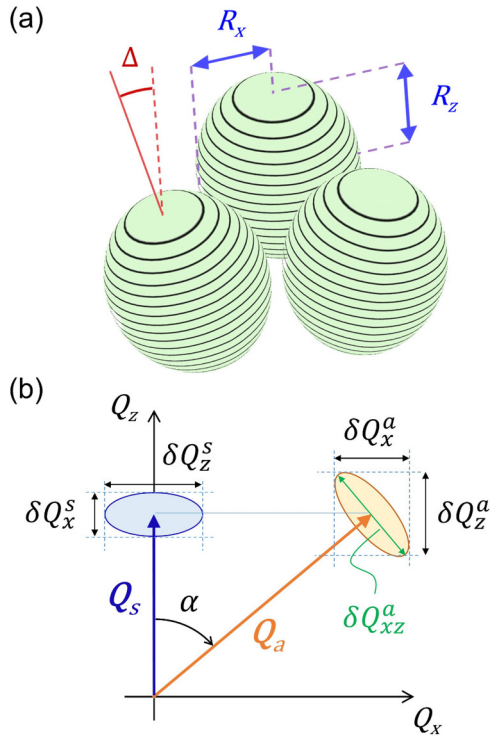


FIG. 5. (a) Mosaic block model utilized to describe the diffuse x-ray scattering from FeRh films. Mosaic blocks with spheroidal shape are considered ( $R_x = R_y \neq R_z$ ). (b) Definition of symmetric and asymmetric diffraction spots in reciprocal space, depicting the peak parameters extracted from experimental data (see main text for details).

the mean block radii ( $R_x$ ,  $R_z$ ) and the mean root square misorientation  $\Delta$  [see Fig. 5(a)]. Although the relation with actual crystal lattice parameters (e.g., density of dislocations) is only indirect, the mosaic block model is a useful mathematical tool to model diffuse x-ray scattering from relaxed epitaxial layers.

The information obtained from reciprocal space map measurements as an input to the mosaic block model is summarized in the schematics of Fig. 5(b). Symmetric and asymmetric diffuse x-ray reflections are sketched in the ( $Q_x$ ,  $Q_z$ ) plane with their position being indicated by the reciprocal space vectors  $Q_s$  and  $Q_a$ , respectively. For relaxed films and spheroid-shaped blocks, one can assume that the intensity contours of the x-ray reflection in reciprocal space have nearly elliptical shapes. The main axes of the ellipse are perpendicular and parallel to the diffraction vectors  $Q_s$  and  $Q_a$  [60].

For a symmetric reflection, the mean block size  $R_z$  in the out-of-plane direction is related to the peak width  $\delta Q_z^s$  [see Fig. 5(b)] via

$$R_z \sim \frac{1}{\delta Q_z^s}. \quad (1)$$

In addition, the peak width  $\delta Q_x^s$  [see Fig. 5(b)] is proportional to [60]

$$\sqrt{\frac{1}{R_x^2} + \frac{(Q_s \Delta)^2}{6}}, \quad (2)$$

where  $R_x$  is the in-plane mosaic block radius and  $\Delta$  the mean quadratic misorientation. Correspondingly, we can distinguish two scenarios for the peak width along the  $x$  orientation. If the blocks are large and strongly misoriented ( $Q_s R \Delta \gg 1$ ), the quantity  $\delta Q_x^s$  is mainly influenced by the misorientation  $\Delta$ . On the other hand, if misorientation is small,  $\delta Q_x^s$  will be indicative of the mosaic block size in the lateral direction.

In the case of an asymmetric reflection, the effect of misorientation is now perceived along both  $Q_x$  and  $Q_z$  axes, as it influences the peak width along the orientation perpendicular to the diffraction vector  $Q_a = Q_a \sin \alpha \hat{i} + Q_a \cos \alpha \hat{k}$  [see Fig. 5(b)]. The elliptical axis of the peak along this orientation is then  $\delta Q_{xz}^a = \sqrt{(\delta Q_x^a)^2 + (\delta Q_z^a)^2}$ . Upon knowledge of the peak widths  $\delta Q_x^s$  and  $\delta Q_{xz}^a$ , we obtain the following system of equations,

$$\begin{aligned} \frac{1}{R_x^2} + \frac{Q_s^2 \Delta^2}{6} &= (\delta Q_x^s)^2, \\ \frac{1}{R_x^2} \cos \alpha + \frac{1}{R_z^2} \sin \alpha + \frac{Q_a^2 \Delta^2}{6} &= (\delta Q_{xz}^a)^2, \end{aligned} \quad (3)$$

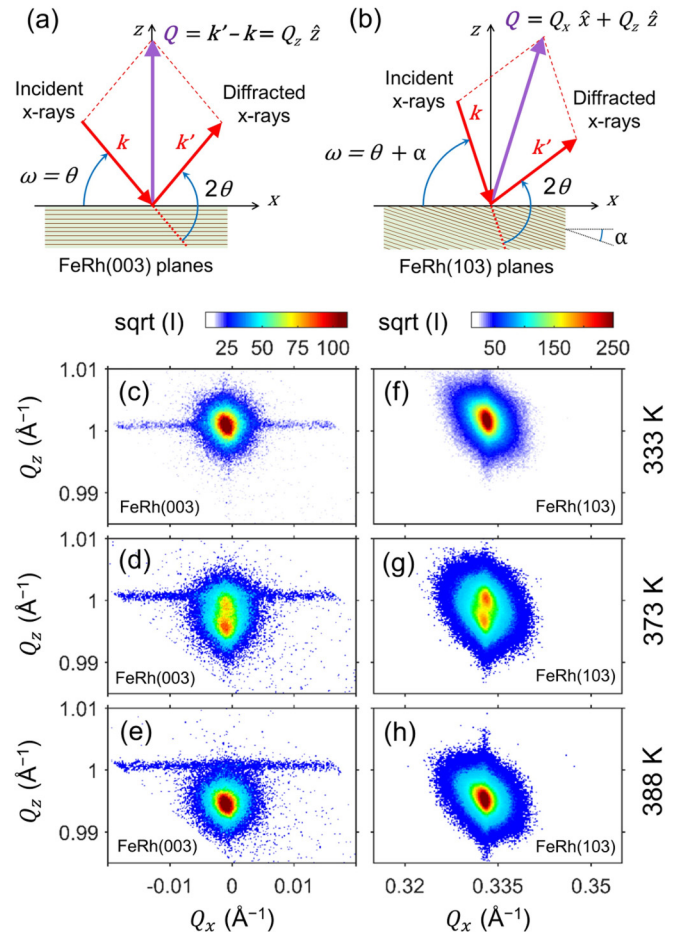


FIG. 6. Schematic of the measurement configuration employed to acquire reciprocal space maps in the FeRh/MgO sample for (a) the symmetric FeRh(003) peak ( $\omega = 50.45^\circ$ ,  $2\theta = 100.90^\circ$ ) and (b) the asymmetric FeRh(103) peak ( $\omega = 72.80^\circ$ ,  $2\theta = 108.84^\circ$ ). Exemplary data sets across the phase transition upon heating are shown (c–e) for FeRh(003) and (f–h) for FeRh(103). The temperatures for the data sets are indicated on the right-hand side.

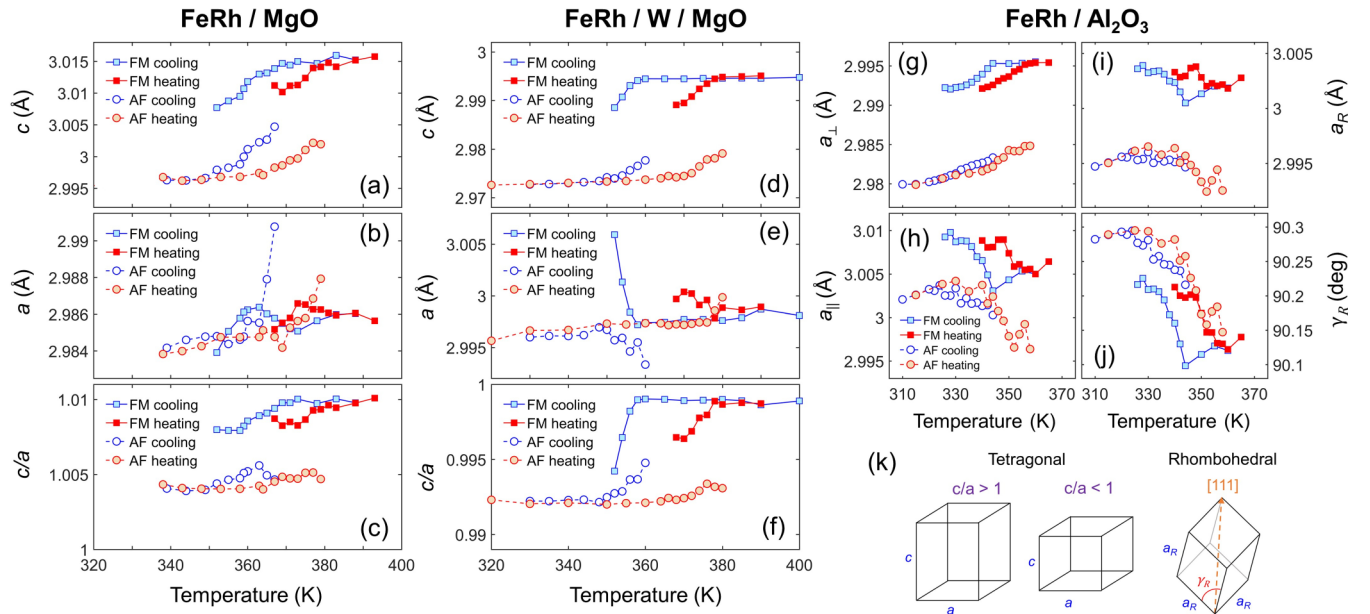


FIG. 7. Temperature dependence of out-of-plane lattice parameter  $c$ , in-plane lattice parameter  $a$ , and tetragonal lattice distortion  $c/a$  for the AF/FM phase fraction during heating and cooling in the (a–c) FeRh/MgO and (d–f) FeRh/W/MgO films. Temperature-dependent (g) out-of-plane and (h) in-plane projections of the rhombohedral lattice parameter in the FeRh/Al<sub>2</sub>O<sub>3</sub> film. (i,j) show the specific temperature dependence of the rhombohedral parameter  $a_R$  and the rhombic angle  $\gamma_R$ . (k) Schematics and definition of the lattice parameters for films with tetragonal and rhombohedral lattice distortions.

where  $R_x$  and  $\Delta$  can be solved, given that  $R_z$  is computed from Eq. (1).

Exemplary temperature-dependent reciprocal space maps for symmetric (left panel) and asymmetric (right panel) diffraction peaks are shown in Fig. 6 for the FeRh/MgO sample during the heating cycle. Figures 6(a) and 6(b) display the schematics of the measurement configuration utilized for retrieving reciprocal space maps from the FeRh(003) and FeRh(103) reflections, respectively. The low- and high-temperature phases are characterized by a single diffraction spot, while splitting of the peak occurs at intermediate temperatures [Figs. 6(d) and 6(g)], corresponding to phase coexistence. The peak splitting is prominent along  $Q_z$ , whereas barely no splitting [Fig. 6(d)] or moderate splitting [Fig. 6(g)] is present along  $Q_x$  for the symmetric and asymmetric reflections scans, respectively.

We acquired extended sets of reciprocal space maps on all FeRh/MgO, FeRh/W/MgO, and FeRh/Al<sub>2</sub>O<sub>3</sub> samples during the heating and cooling cycles using temperature steps of 5 K and finer steps of 2 K in the transition region. We focused on the FeRh(003) and FeRh(103) diffraction peaks for films on MgO and W/MgO, whereas the FeRh(222) and FeRh(112) peaks were followed for the film on Al<sub>2</sub>O<sub>3</sub> [49]. The diffraction peaks from all reciprocal space map data sets were fitted using two-dimensional Gaussian peaks, from which the peak center and width was extracted. For simplicity, we assumed that the width of the diffraction peaks along the  $Q_z$  direction is equal for both the AF and FM phases; i.e., the mosaic block model does not account for phase fragmentation across the thickness of the film. The assumption is well justified in the case of well-ordered epitaxial films in which nearly the entire thickness of the film coherently scatters x rays [43]. Using the peak center data, the results from symmetric and asymmetric

scans were combined in order to correct for slight sample misorientations that may occur during the temperature scans. Technically, we imposed  $Q_x = 0$  for the symmetric diffraction peaks at each temperature and propagated the corrected tilt to the asymmetric diffraction peaks. From here, we obtain phase-resolved (AF or FM) out-of-plane and in-plane lattice parameter data across the entire transition.

The temperature-dependent phase-specific lattice parameter data are shown in Fig. 7. For the tetragonally distorted FeRh films on MgO and W/MgO, the out-of-plane lattice parameter  $c$  [Figs. 7(a) and 7(d), respectively] follows monotonic trends with temperature for both AF and FM phases. AF and FM lattices expand upon heating and contract upon cooling along the out-of-plane direction, thus following the action of temperature-induced stress. The out-of-plane lattice expansion accounts for the majority of volume increase across the transition ( $\Delta c \sim 0.02$  Å). The  $c$  parameter shows well separated values for the AF and FM phase, following a hysteresis in temperature when comparing the heating and cooling cycles.

Additionally, the temperature-dependent in-plane lattice parameter data for FeRh/MgO and FeRh/W/MgO are shown in Figs. 7(b) and 7(e). The  $a$ -parameter variation upon comparing the pure AF and FM phases is far more limited than that of the  $c$  parameter ( $\Delta a \sim 0.004$  Å; see also Table I). This is due to the limited ability of the lattice to accommodate larger volume changes along the in-plane direction as a consequence of the epitaxial clamping to the substrate.

Contrary to the  $c$  parameter, we find that the  $a$  parameter does not follow a monotonic trend with temperature, but shows more complex behavior during phase coexistence. For FeRh/MgO [Fig. 7(b)], both AF and FM  $a$  parameters grow during heating after the appearance of the FM phase at 367 K.



However, the FM  $a$  parameter starts decreasing upon heating above 373 K while the AF  $a$  parameter continues to grow. Before the transition is completed, the minority AF film fraction shows a larger  $a$  parameter than the complementary FM phase. An equivalent kink in  $a$  is apparent for the FM phase upon cooling. The AF  $a$  parameter initially shrinks while the FM one grows as temperature decreases. Below 362 K the FM  $a$  parameter changes its trend and both phases shrink in plane upon cooling (see Fig. 7(b) and Supplemental Material [49]).

These trends can be qualitatively explained in terms of the different stress contributions to which the in-plane lattice parameter responds. While temperature-induced stress generally causes an isotropic lattice expansion upon heating, the compressive in-plane stress exerted by the MgO substrate is anisotropic in nature. The substrate prevents further in-plane expansion of the FM phase upon heating as a larger film fraction transitions from the AF phase. Consequently, the trend is reversed and the FM  $a$  parameter slightly decreases upon further heating. Additionally, the slight in-plane contraction of the FM phase is in line with the Poisson effect, which favors in-plane contraction upon the relatively large expansion in the out-of-plane direction. Finally, the lateral mechanical coupling between crystallographic grains in the film has to be taken into account as well. FM grain contraction seems to be balanced by a sharp increase of the AF  $a$  parameter in the regions where the AF constitutes the minority phase fraction, during both heating and cooling [Fig. 7(b)].

The in-plane lattice parameter data for the FeRh/W/MgO reflects a similar situation as for FeRh/MgO, except for the fact that the substrate now induces in-plane tensile strain. Apparently this causes the AF and FM  $a$  parameters to follow opposite trends during heating but not during cooling. While the AF lattice expands in plane during heating, the FM lattice contracts. During cooling, however, both AF and FM lattices expand (see Fig. 7(e) and Supplemental Material [49]), with a considerable increase of the  $a$  parameter in the FM phase ( $3.0056 \pm 0.0006$  nm at 352 K) just before disappearing. This in-plane expansion partially balances the reduced  $a$  parameter of the emergent AF phase upon cooling, in line with the tensile in-plane stress applied by the W/MgO substrate.

The different behavior observed in FeRh/MgO and FeRh/W/MgO can also be analyzed with respect to the tetragonal distortion ratio  $c/a$  [Figs. 7(c) and 7(f)]. For FeRh/MgO,  $c/a$  ranges between 1.004 and 1.010; i.e. characteristic compressive in-plane strain is present for both AF and FM phases. The tetragonal deformation is more pronounced in the FM phase. Conversely, the ratio  $c/a$  for FeRh/W/MgO remains below 1 at all temperatures [Fig. 7(f)]. Here, the deformation is largest in the AF phase, whereas  $c/a$  is very close to 1 within the fully FM phase ( $\sim 0.999$ ). The ratio  $c/a$  approaching 1 in either phase could be linked to a larger ability of the lattice to act upon the combined presence of temperature- and substrate-induced stresses. This is due to the reduced deformation restriction imposed by the Poisson effect when the lattice adopts the most stable cubic configuration. It is worth noting that despite the very different  $c/a$  ratios, both FeRh/MgO and FeRh/W/MgO show equivalent unit cell volumes in fully AF and FM phases (see Supplemental Material [49]).

For the FeRh film on  $\text{Al}_2\text{O}_3$ , we have obtained the out-of-plane and in-plane projections of the rhombohedral lattice

parameter,  $a_{\perp}$  and  $a_{\parallel}$ , which are shown in Figs. 7(g) and 7(h). The rhombohedral lattice parameter  $a_R$  and the rhombic angle  $\gamma_R$  [see schematics in Fig. 7(k)] are subsequently obtained from these projections as

$$a_R = \sqrt{\frac{a_{\perp}^2 + 2a_{\parallel}^2}{3}}, \quad \cos \gamma_R = \frac{a_{\perp}^2 - a_{\parallel}^2}{a_{\perp}^2 + 2a_{\parallel}^2}, \quad (4)$$

and have been plotted for different temperatures in Figs. 7(i) and 7(j). A significant change in the lattice parameter  $a_R$  is observed between the AF and FM phases ( $\Delta a_R \sim 0.01 \text{ \AA}$ ), which accounts for the majority of the volume expansion across the AF-to-FM phase transition. At the same time, a gradual reduction of the rhombic angle  $\gamma_R$  between  $90.28 \pm 0.04^\circ$  and  $90.14 \pm 0.05^\circ$  with increasing temperature [Fig. 7(j)] accommodates the lattice expansion as well. Compared to the films on MgO and W/MgO, the FeRh/ $\text{Al}_2\text{O}_3$  film shows a larger lattice volume of the AF and FM phases (see Supplemental Material [49]), which is in line with the observed reduction in phase transition temperature.

Furthermore, the average mosaic block size (or crystalline coherence length in terms of the grain size) across the thermally driven transition has been obtained for the FeRh films on different substrates. The fitted horizontal and vertical grain sizes of the AF and FM regions are shown in Fig. 8, in terms of the grain radii  $R_x$  and  $R_z$ , respectively. Figure 8(a) indicates that the lateral grain size (twice the radius) in FeRh/MgO is about  $\sim 60$  nm in both AF and FM phases ( $60.8 \pm 0.3$  nm at 334 K), while this value decreases down to  $\sim 22$  nm in the transition region. Remarkably, these numbers are in excellent agreement with the typical nucleation volume corresponding to discrete resistance jumps measured across the AF-to-FM transition in mesoscale FeRh stripes. The largest activation volume was estimated to be about  $1.65 \times 10^{-4} \mu\text{m}^3$ , which corresponds to an in-plane grain size of 59 nm [47].

The  $R_z$  data in Fig. 8(b) show that the vertical grain size in both phases is comparable to the film thickness ( $48.4 \pm 0.5$  nm), while there is a reduction during phase coexistence, analogous to the horizontal grain size behavior. A slight difference between the AF vertical grain size  $2R_z$  ( $42.2 \pm 0.3$  nm at 334 K) and the FM one ( $45.8 \pm 0.2$  nm at 393 K) emerges when comparing data below and above the phase transition. The difference of around 3 nm corresponds to the thickness of FM interfacial layers at the film-substrate and film-capping boundaries, which are present in the AF phase. This effect has been previously identified using polarized neutron reflectometry and x-ray photoemission techniques directly probing the magnetic order [38,52,53]. Here, the interfacial FM regions do not coherently scatter with the AF majority fraction of the film, but they do when the entire film becomes FM above the phase transition. This confirms that the grain size analysis via XRD can be used to quantify the interfacial FM phase thickness in FeRh.

The grain size data for FeRh/W/MgO are shown in Figs. 8(c) and 8(d). The horizontal mosaic block size vs temperature shows a similar behavior as for FeRh/MgO. However, in this case the lateral crystalline coherence length is about  $17.2 \pm 0.8$  nm (at 310 K), significantly lower than in FeRh/MgO. The decrease in grain size upon phase

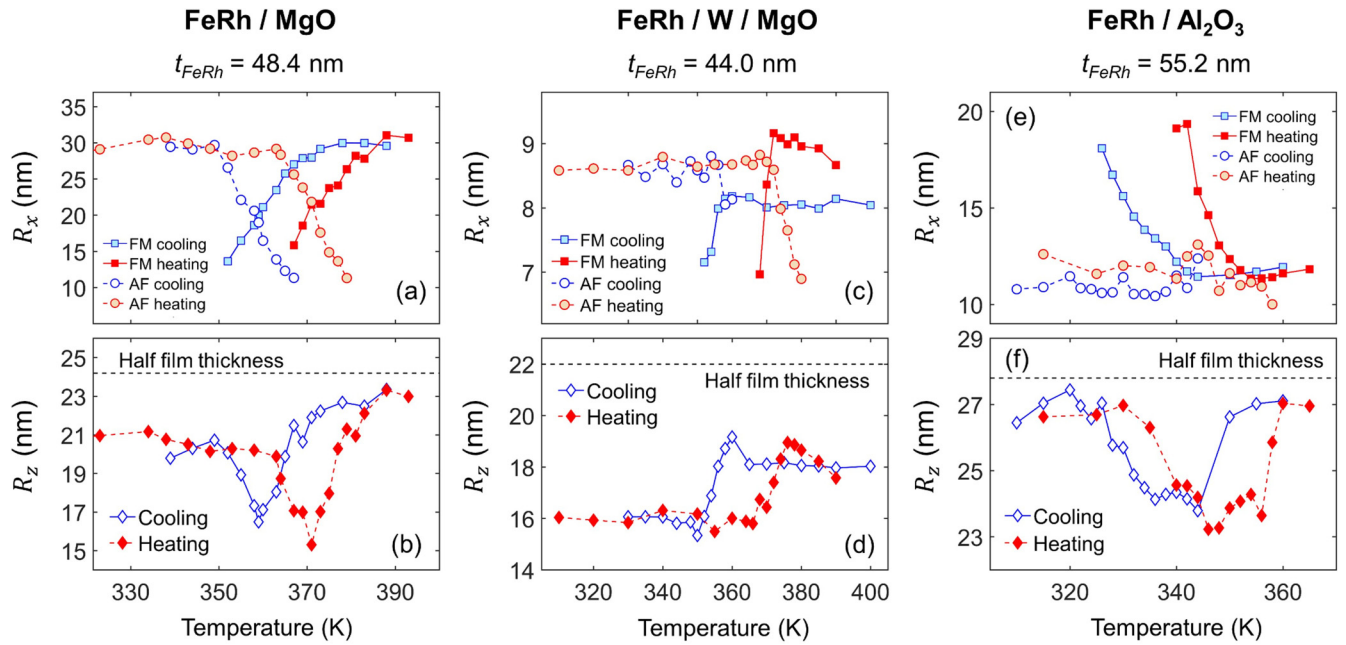


FIG. 8. Temperature-dependent in-plane (top panel) and out-of-plane (bottom panel) grain size in terms of the mosaic block radius as extracted from the model described in the main text, for (a,b) FeRh/MgO, (c,d) FeRh/W/MgO, and (e,f) FeRh/Al<sub>2</sub>O<sub>3</sub>. The horizontal dashed lines in (b,d,f) are indicative of the film half thickness in each case.

coexistence is very abrupt, indicating that the film shows a high degree of AF/FM domain fragmentation during both cooling and heating. On the other hand, the vertical grain size ( $32.1 \pm 0.2$  nm at 310 K) is smaller than the film thickness of  $44.02 \pm 0.02$  nm [Fig. 8(d)], which points to a certain loss of crystalline coherence integrity or a non-negligible strain gradient across the thickness of the film. The data indicate a difference of about 4 nm between the grain size in the FM and AF phases, which can be again explained in terms of the contribution of the FM stabilized regions in the low-temperature phase. Surprisingly, phase coexistence does not present any substantial reduction in the vertical grain size.

Finally, the FeRh film on Al<sub>2</sub>O<sub>3</sub> [Fig. 8(e)] features a constant lateral grain size of about  $\sim 22$  nm ( $21.6 \pm 0.2$  nm at 310 K) in the AF phase at all temperatures. This is in contrast to the FM phase in which the grain size increases up to  $\sim 35$  nm during phase coexistence. The vertical grain size of  $52.9 \pm 0.1$  nm at 310 K [Fig. 8(f)] is slightly smaller when compared to the film thickness of  $55.2 \pm 0.2$  nm. This discrepancy may arise from the presence of a weak fcc-FeRh fraction at the interface between the film and substrate, which was also apparent in symmetric x-ray scans [Fig. 2(c)].

The mosaic block model was also employed to determine the mean quadratic misorientation  $\Delta$  of the crystallites in the studied films. The obtained  $\Delta$  values were  $0.18 \pm 0.02^\circ$ ,  $0.6 \pm 0.1^\circ$ , and  $0.7 \pm 0.2^\circ$  for the FeRh films on MgO, W/MgO, and Al<sub>2</sub>O<sub>3</sub>, respectively, indicating larger misorientation for larger film-substrate mismatch.

#### D. Strain asymmetry during heating and cooling

A characteristic feature of FeRh films as opposed to the bulk case is that the transition broadens due to the presence

of crystallographic defects and local stoichiometry variations. As different parts of the sample possess slightly different transition temperatures, coexistence of AF and FM domains occurs [46], leading to smearing out of the sharp, first-order phase transition. Some studies have found modest signatures of asymmetry in films when comparing the cooling and heating cycles, in terms of phase separation and domain nucleation kinetics [43,61]. Recently, Uhlíř *et al.* found a giant asymmetry of the phase transition in patterned submicron FeRh stripes while measuring their temperature-dependent resistance. While a broad transition was observed upon heating, a collective response featuring a transition in few abrupt jumps appeared during cooling [47]. Complementary magneto-optical Kerr effect experiments confirmed that the asymmetry is present when tracking the magnetization order parameter as well [62]. The origin of this asymmetry was attributed to the fact that while long-range FM order can persist through regions of disorder, long-range AF order is easily disrupted by defects, such as crystallographic site swapping or grain boundaries. The asymmetry is more prominent upon spatial confinement, as FM exchange interaction efficiently stabilizes the high-temperature phase and favors a collective FM-to-AF transition. In the reverse AF-to-FM transition, the shorter AF exchange correlations cannot prevent fragmented gradual transformation.

Related behavior can be observed here in the strain of the FM phase, as the lattice in the high-temperature phase is typically more deformed during cooling than heating. This is apparent, for instance, from the out-of-plane lattice parameter data in Figs. 7(a) and 7(d). In order to better visualize this difference in the strain value, we acquired very high signal-to-noise ratio symmetric x-ray scans on two FeRh/MgO films of different thicknesses. Figure 9(a) exhibits *c* parameter data

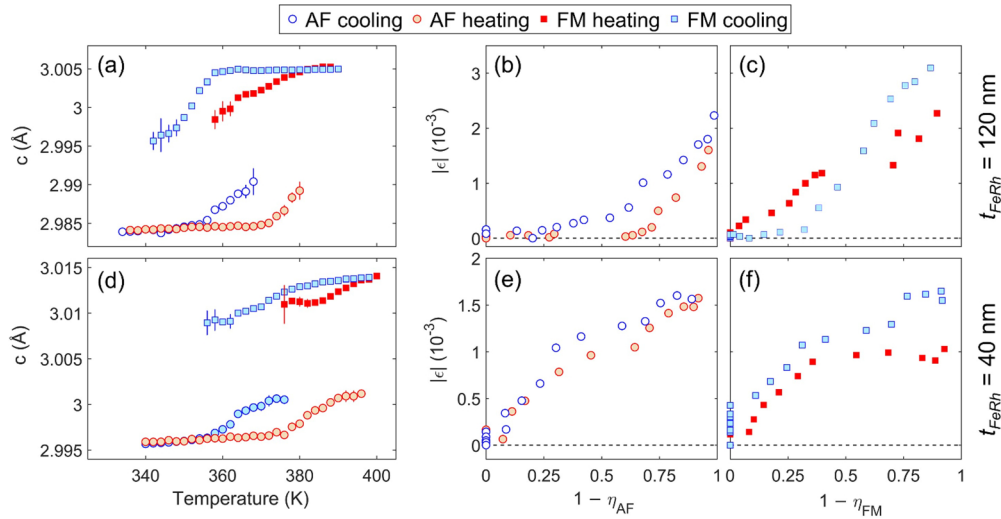


FIG. 9. (a) Temperature dependence of the out-of-plane lattice parameter for the AF/FM phases during heating/cooling for a 120-nm-thick epitaxial FeRh film on MgO. (b,c) indicate the absolute value of phase-specific strain vs the complementary phase fraction  $1-\eta$  for the AF and FM phases, respectively. (d–f) display the same type of data measured for a 40-nm-thick FeRh film on MgO. Exemplary error bars are included in (a,d).

for the AF and FM phases in a 120-nm-thick FeRh film, which has been measured with 2 K resolution. It is evident that the FM phase fraction reaches smaller  $c$  values during the cooling cycle, while the AF phase fraction shows similar maximum values of  $c$  during both heating and cooling. This suggests that the FM phase can stand larger deformation, being effectively supercooled before transitioning to the low-temperature phase. It is useful to represent the phase-specific strain<sup>4</sup> as a function of the relative fraction of the complementary phase, as in Figs. 9(b) and 9(c). In Figure 9(b), data points representing the relative strain of the AF phase are shown as a function of the remaining FM phase fraction,<sup>5</sup>  $1 - \eta_{AF}$ . The data show a gradual, monotonic increase of strain in the AF phase as its relative fraction in the film increases. The maximum relative strain reaches a highest value of  $\sim 2 \times 10^{-3}$  during both heating and cooling. In the case of the FM phase, however, we find a strain asymmetry when comparing the cooling ( $\sim 3 \times 10^{-3}$ ) and heating ( $\sim 2 \times 10^{-3}$ ) cycles at those stages where the FM phase constitutes a minority fraction in the system.

The ability to stand larger deformation can be linked to the more robust character of the FM exchange interaction in the presence of ubiquitous defects in the films. On the contrary, short-distance AF correlations lead to small domains with coherent AF ordering [63]. While this difference in magnetic correlations shows most remarkable effects only upon nanoscale geometrical confinement of FeRh [47,62], it is still observable in the structural properties of thin films, despite its signatures being subtler [43].

Analogous data sets are presented in Figs. 9(d)–9(f) for a 40-nm-thick FeRh film, where the maximum strain observed in the FM phase is also larger during cooling than in the heating cycle ( $\sim 1.7 \times 10^{-3}$  vs  $\sim 1 \times 10^{-3}$ ). The strain levels for the minority AF phase are again comparable. One can also notice that the strain dependence on the complementary phase fraction [Figs. 9(e) and 9(f)] shows a slightly different trend, reaching saturation as  $1 - \eta$  approaches 1. This is an indication of larger mechanical coupling to the substrate (the thinner film is less relaxed), making the AF and FM phase lattices less susceptible to accommodate the strain exerted upon temperature variations.

#### IV. CONCLUSIONS

In conclusion, we have investigated the temperature-dependent structural properties of AF and FM phases in epitaxial FeRh films grown on different substrates (MgO, W/MgO, Al<sub>2</sub>O<sub>3</sub>). The three substrates induce different tetragonal ( $c/a > 1$  and  $c/a < 1$ ) or rhombohedral distortions. In combination with appropriate buffer layers, the  $c/a$  value in tetragonally distorted films can be tuned in the range of 0.99–1.01 while preserving the phase transition above room temperature. Similarly, the effect of strain relaxation on the phase transition temperature upon varying the film thickness was inspected for all substrate systems. Reciprocal space map measurements for films of comparable thickness on all the substrates were acquired, resolving the phase-specific structural information in great detail. The lattice parameters as well as the crystalline coherence lengths in terms of grain sizes were determined in the out-of-plane and in-plane directions of the film across the phase transition. The crystalline coherence length analysis of phases above and below the transition temperature identified that the out-of-plane AF grain size is smaller than the FeRh film thickness by 3 nm. This can be associated with the persistence of ultrathin interfacial FM

<sup>4</sup>The strain values here are defined as phase specific; i.e., the quantity  $\epsilon$  for the AF and FM phase is defined as the deformation with respect to the values at lowest and highest temperatures, respectively.

<sup>5</sup> $\eta_{AF}, \eta_{FM}$  are defined such that  $\eta_{AF} + \eta_{FM} = 1$ .

regions at room temperature, which is in agreement with available depth-resolved polarized neutron reflectometry studies. Finally, we found that the FM phase fraction is considerably more strained during the transition upon cooling (by about 30%), whereas the maximum strain level in the AF phase was identical during both heating and cooling. We suggest that this observation is linked to the larger FM correlation length (as compared to the AF one) when initiating the transition from a pure FM phase.

The observations presented here reflect fine details of the structural interplay between AF and FM phases in FeRh films with a great variety of achievable lattice distortions. This could also be useful as an input for theoretical calculations, which have recently aimed towards unveiling hidden

strain-dependent magnetostructural transitions in this material [64–66].

### ACKNOWLEDGMENTS

We thank Eric Fullerton for fruitful discussions and constructive feedback on the manuscript. We acknowledge the Grant Agency of the Czech Republic (Grant No. 16-23940Y). We acknowledge the CzechNanoLab Research Infrastructure supported by MEYS CR (LM2018110). This work has received funding from the European Union's Horizon 2020 research and innovation program under the Marie Skłodowska-Curie and it is cofinanced by the South Moravian Region under Grant Agreement No. 665860.

- 
- [1] D. Sander, S. O. Valenzuela, D. Makarov, C. H. Marrows, E. Fullerton, P. Fischer, J. McCord, P. Vavassori, S. Mangin, P. Pirro, B. Hillebrands, A. D. Kent, T. Jungwirth, O. Gutfleisch, C. G. Kim, and A. Berger, The 2017 magnetism roadmap, *J. Phys. D: Appl. Phys.* **50**, 363001 (2017).
- [2] M. R. Ibarra and P. A. Algarabel, Giant volume magnetostriction in the FeRh alloy, *Phys. Rev. B* **50**, 4196 (1994).
- [3] L. Morellon, J. Stankiewicz, B. García-Landa, P. A. Algarabel, and M. R. Ibarra, Giant magnetoresistance near the magnetostructural transition in  $Gd_5(Si_{1.8}Ge_{2.2})$ , *Appl. Phys. Lett.* **73**, 3462 (1998).
- [4] M. Pasquale, C. P. Sasso, L. H. Lewis, L. Giudici, T. Lograsso, and D. Schlögl, Magnetostructural transition and magnetocaloric effect in  $Ni_{55}Mn_{20}Ga_{25}$  single crystals, *Phys. Rev. B* **72**, 094435 (2005).
- [5] E. Liu, W. Wang, L. Feng, W. Zhu, G. Li, J. Chen, H. Zhang, G. Wu, C. Jiang, H. Xu, and F. de Boer, Stable magnetostructural coupling with tunable magneto-responsive effects in hexagonal ferromagnets, *Nat. Commun.* **3**, 873 (2012).
- [6] H. Yan, Z. Feng, S. Shang, X. Wang, Z. Hu, J. Wang, Z. Zhu, H. Wang, Z. Chen, H. Hua, W. Lu, J. Wang, P. Qin, H. Guo, X. Zhou, Z. Leng, Z. Liu, C. Jiang, M. Coey, and Z. Liu, A piezoelectric, strain-controlled antiferromagnetic memory insensitive to magnetic fields, *Nat. Nanotechnol.* **14**, 131 (2019).
- [7] S. B. Roy, First order magneto-structural phase transition and associated multi-functional properties in magnetic solids, *J. Phys.: Condens. Matter* **25**, 183201 (2013).
- [8] M. Fallot and R. Hocart, Sur l'apparition du ferromagnétisme par élévation de température dans des alliages de fer et de rhodium, *Rev. Sci.* **77**, 498 (1939).
- [9] G. Shirane, R. Nathans, and C. W. Chen, Magnetic moments and unpaired spin densities in the Fe-Rh alloys, *Phys. Rev.* **134**, A1547 (1964).
- [10] A. I. Zakharov, A. M. Kadomtseva, R. Z. Levitin, and E. G. Ponyatovskii, Magnetic and magnetoelastic properties of a metamagnetic iron-rhodium alloy, *Sov. Phys. - JETP* **19**, 1348 (1964).
- [11] V. L. Moruzzi and P. M. Marcus, Antiferromagnetic-ferromagnetic transition in FeRh, *Phys. Rev. B* **46**, 2864 (1992).
- [12] J. S. Kouvel and C. C. Hartelius, Anomalous magnetic moments and transformations in the ordered alloy FeRh, *J. Appl. Phys.* **33**, 1343 (1962).
- [13] L. H. Lewis, C. H. Marrows, and S. Langridge, Coupled magnetic, structural and electronic phase transitions in FeRh, *J. Phys. D: Appl. Phys.* **49**, 323002 (2016).
- [14] S. Maat, J.-U. Thiele, and E. E. Fullerton, Temperature and field hysteresis of the antiferromagnetic-to-ferromagnetic phase transition in epitaxial FeRh films, *Phys. Rev. B* **72**, 214432 (2005).
- [15] I. Suzuki, M. Itoh, and T. Taniyama, Elastically controlled magnetic phase transition in Ga-FeRh/BaTiO<sub>3</sub>(001) heterostructure, *Appl. Phys. Lett.* **104**, 022401 (2014).
- [16] R. O. Cherifi, V. Ivanovskaya, L. C. Phillips, A. Zobelli, I. C. Infante, E. Jacquet, V. Garcia, S. Fusil, P. R. Briddon, N. Guiblin, A. Mougin, A. A. Ůnal, F. Kronast, S. Valencia, B. Dkhil, A. Barthélémy, and M. Bibes, Electric-field control of magnetic order above room temperature, *Nat. Mater.* **13**, 345 (2014).
- [17] N. Matsuzaki, T. Moriyama, M. Nagata, K.-J. Kim, I. Suzuki, T. Taniyama, and T. Ono, Current induced antiferromagnetic transition in FeRh nanowires, *Jpn. J. Appl. Phys.* **54**, 073002 (2015).
- [18] J.-U. Thiele, M. Buess, and C. H. Back, Spin dynamics of the antiferromagnetic-to-ferromagnetic phase transition in FeRh on a sub-picosecond time scale, *Appl. Phys. Lett.* **85**, 2857 (2004).
- [19] G. Ju, J. Hohlfeld, B. Bergman, R. J. M. van de Veerdonk, O. N. Mryasov, J.-Y. Kim, X. Wu, D. Weller, and B. Koopmans, Ultrafast Generation of Ferromagnetic Order via a Laser-Induced Phase Transformation in FeRh Thin Films, *Phys. Rev. Lett.* **93**, 197403 (2004).
- [20] S. O. Mariager, F. Pressacco, G. Ingold, A. Caviezel, E. Möhr-Vorobeva, P. Beaud, S. L. Johnson, C. J. Milne, E. Mancini, S. Moyerman, E. E. Fullerton, R. Feidenhans'l, C. H. Back, and C. Quitmann, Structural and Magnetic Dynamics of a Laser Induced Phase Transition in FeRh, *Phys. Rev. Lett.* **108**, 087201 (2012).
- [21] F. Quirin, M. Vattilana, U. Shymanovich, A.-E. El-Kamhawy, A. Tarasevitch, J. Hohlfeld, D. von der Linde, and K. Sokolowski-Tinten, Structural dynamics in FeRh during a laser-induced metamagnetic phase transition, *Phys. Rev. B* **85**, 020103(R) (2012).
- [22] F. Pressacco, V. Uhlíř, M. Gatti, A. Nicolaou, A. Bendounan, J. A. Arregi, S. K. K. Patel, E. E. Fullerton, D. Krizmancic, and F. Sirotti, Laser induced phase transition in epitaxial FeRh layers

- studied by pump-probe valence band photoemission, *Struct. Dyn.* **5**, 034501 (2018).
- [23] J.-U. Thiele, S. Maat, and E.E. Fullerton, FeRh/FePt exchange spring films for thermally assisted magnetic recording media, *Appl. Phys. Lett.* **82**, 2859 (2003).
- [24] X. Marti, I. Fina, C. Frontera, J. Liu, P. Wadley, Q. He, R. J. Paull, J. D. Clarkson, J. Kudrnovský, I. Turek, J. Kuneš, D. Yi, J.-H. Chu, C. T. Nelson, L. You, E. Arenholz, S. Salahuddin, J. Fontcuberta, T. Jungwirth, and R. Ramesh, Room-temperature antiferromagnetic memory resistor, *Nat. Mater.* **13**, 367 (2014).
- [25] M. P. Annaorazov, K. A. Asatryan, G. Myalikgulyev, S. A. Nikitin, A. M. Tishin, and A. L. Tyurin, Alloys of the Fe-Rh system as a new class of working material for magnetic refrigerators, *Cryogenics* **32**, 867 (1992).
- [26] V. Uhlřf, F. Pressacco, J. A. Arregi, P. Procházka, S. Průša, M. Potoček, T. Šikola, J. Čechal, A. Bendounan, and F. Sirotti, Single-layer graphene on epitaxial FeRh thin films, *Appl. Surf. Sci.* **514**, 145923 (2020).
- [27] J. Cao, N. T. Nam, S. Inoue, H. Y. Y. Ko, N. Y. Phuoc, and T. Suzuki, Magnetization behaviors for FeRh single crystal thin films, *J. Appl. Phys.* **103**, 07F501 (2008).
- [28] A. Chirkova, F. Bittner, K. Nenkov, N. V. Baranov, L. Schultz, K. Nielsch, and T. G. Woodcock, The effect of microstructure on the antiferromagnetic to ferromagnetic transition in FeRh alloys, *Acta Mater.* **131**, 31 (2017).
- [29] C. W. Barton, T. A. Ostler, D. Huskisson, C. J. Kinane, S. J. Haigh, G. Hrkac, and T. Thomson, Substrate induced strain field in FeRh epilayers grown on single crystal MgO (001) substrates, *Sci. Rep.* **7**, 44397 (2017).
- [30] Y. Ohtani and I. Hatakeyama, Antiferro-ferromagnetic transition and microstructural properties in a sputter deposited FeRh thin film system, *J. Appl. Phys.* **74**, 3328 (1993).
- [31] Y. Ohtani and I. Hatakeyama, Features of broad magnetic transition in FeRh thin film, *J. Magn. Magn. Mater.* **131**, 339 (1994).
- [32] C. Bordel, J. Juraszek, D. W. Cooke, C. Baldasseroni, S. Mankovsky, J. Minár, H. Ebert, S. Moyerman, E. E. Fullerton, and F. Hellman, Fe Spin Reorientation across the Metamagnetic Transition in Strained FeRh Thin Films, *Phys. Rev. Lett.* **109**, 117201 (2012).
- [33] J.-S. Lee, E. Vescovo, L. Plucinski, C. M. Schneider, and C.-C. Kao, Electronic structure and magnetic properties of epitaxial FeRh(001) ultrathin films on W(100), *Phys. Rev. B* **82**, 224410 (2010).
- [34] P. Drózdź, M. Ślęzak, K. Matlak, B. Matlak, K. Freindl, D. Wilgocka-Ślęzak, N. Spiridis, J. Korecki, and T. Ślęzak, Switching of Co Magnetization Driven by Antiferromagnetic-Ferromagnetic Phase Transition of FeRh Alloy in Co/FeRh Bilayers, *Phys. Rev. Appl.* **9**, 034030 (2018).
- [35] S. Yamada, K. Tanikawa, J. Hirayama, T. Kanashima, T. Taniyama, and K. Hamaya, Low-temperature B2 ordering and magnetic properties of Fe<sub>100-x</sub>Rh<sub>x</sub> films on bcc alloys, *Phys. Rev. B* **92**, 094416 (2015).
- [36] A. Ceballos, Z. Chen, O. Schneider, C. Bordel, L.-W. Wang, and F. Hellman, Effect of strain and thickness on the transition temperature of epitaxial FeRh thin-films, *Appl. Phys. Lett.* **111**, 172401 (2017).
- [37] Y. Lee, Z. Q. Liu, J. T. Heron, J. D. Clarkson, J. Hong, C. Ko, M. D. Biegalski, U. Aschauer, S. L. Hsu, M. E. Nowakowski, J. Wu, H. M. Christen, S. Salahuddin, J. B. Bokor, N. A. Spaldin, D. G. Schlom, and R. Ramesh, Large resistivity modulation in mixed-phase metallic systems, *Nat. Commun.* **6**, 5959 (2015).
- [38] S. P. Bennett, A. T. Wong, A. Glavic, A. Herklotz, C. Urban, I. Valmianski, M. D. Biegalski, H. M. Christen, T. Z. Ward, and V. Lauter, Giant controllable magnetization changes induced by structural phase transitions in a metamagnetic artificial multiferroic, *Sci. Rep.* **6**, 22708 (2016).
- [39] Z. Q. Liu, L. Li, Z. Gai, J. D. Clarkson, S. L. Hsu, A. T. Wong, L. S. Fan, M.-W. Lin, C. M. Rouleau, T. Z. Ward, H. N. Lee, A. S. Sefat, H. M. Christen, and R. Ramesh, Full Electroresistance Modulation in a Mixed-Phase Metallic Alloy, *Phys. Rev. Lett.* **116**, 097203 (2016).
- [40] Q. B. Hu, J. Li, C. C. Wang, Z. J. Zhou, Q. Q. Cao, T. J. Zhou, D. H. Wang, and Y. W. Du, Electric field tuning of magnetocaloric effect in FeRh<sub>0.96</sub>Pd<sub>0.04</sub>/PMN-PT composite near room temperature, *Appl. Phys. Lett.* **110**, 222408 (2017).
- [41] L. Zsoldos, Lattice parameter change of FeRh alloys due to antiferromagnetic-ferromagnetic transformation, *Phys. Status Solidi B* **20**, K25 (1967).
- [42] J.-U. Thiele, S. Maat, J. L. Robertson, and E. E. Fullerton, Magnetic and structural properties of FePt-FeRh exchange spring films for thermally assisted magnetic recording media, *IEEE Trans. Magn.* **40**, 2537 (2004).
- [43] M. A. de Vries, M. Loving, M. McLaren, R. M. D. Brydson, X. Liu, S. Langridge, L. H. Lewis, and C. H. Marrows, Asymmetric “melting” and “freezing” kinetics of the magnetostructural phase transition in B2-ordered FeRh epilayers, *Appl. Phys. Lett.* **104**, 232407 (2014).
- [44] J. W. Kim, P. J. Ryan, Y. Ding, L. H. Lewis, M. Ali, C. J. Kinane, B. J. Hickey, C. H. Marrows, and D. A. Arena, Surface influenced magnetostructural transitions in FeRh films, *Appl. Phys. Lett.* **95**, 222515 (2009).
- [45] C. Gatel, B. Warot-Fonrose, N. Biziere, L.A. Rodríguez, D. Reyes, R. Cours, M. Castiella, and M. J. Casanove, Inhomogeneous spatial distribution of the magnetic transition in an iron-rhodium thin film, *Nat. Commun.* **8**, 15703 (2017).
- [46] D. J. Keavney, Y. Choi, M. V. Holt, V. Uhlřf, D. Arena, E. E. Fullerton, P. J. Ryan, and J.-W. Kim, Phase coexistence and kinetic arrest in the magnetostructural transition of the ordered alloy FeRh, *Sci. Rep.* **8**, 1778 (2018).
- [47] V. Uhlřf, J. A. Arregi, and E. E. Fullerton, Colossal magnetic phase transition asymmetry in mesoscale FeRh stripes, *Nat. Commun.* **7**, 13113 (2016).
- [48] J. del Valle, N. Ghazikhanian, Y. Kalcheim, J. Trastoy, M.-H. Lee, M. J. Rozenberg, and I. K. Schuller, Resistive asymmetry due to spatial confinement in first-order phase transitions, *Phys. Rev. B* **98**, 045123 (2018).
- [49] See Supplemental Material at <http://link.aps.org/supplemental/10.1103/PhysRevB.101.174413> for the multilayer model parameter fits extracted from x-ray reflectivity, details of the optimization of the W buffer layer in FeRh/W/MgO samples, extended data sets, and details concerning the x-ray reciprocal space map measurements, as well as additional aspects of tetragonally distorted FeRh films.
- [50] I. Suzuki, I. Suzuki, Y. Hamasaki, M. Itoh, and T. Taniyama, Controllable exchange bias in Fe/metamagnetic FeRh bilayers, *Appl. Phys. Lett.* **105**, 172401 (2014).
- [51] L. J. Swartzendruber, The Fe-Rh (iron-rhodium) system, *Bull. Alloy Phase Diagr.* **5**, 456 (1984).

- [52] R. Fan, C. J. Kinane, T. R. Charlton, R. Dorner, M. Ali, M. A. de Vries, R. M. D. Brydson, C. H. Marrows, B. J. Hickey, D. A. Arena, B. K. Tanner, G. Nisbet, and S. Langridge, Ferromagnetism at the interfaces of antiferromagnetic FeRh epilayers, *Phys. Rev. B* **82**, 184418 (2010).
- [53] F. Pressacco, V. Uhlíř, M. Gatti, A. Bendounan, E. E. Fullerton, and F. Sirotti, Stable room-temperature ferromagnetic phase at the FeRh(100) surface, *Sci. Rep.* **6**, 22383 (2016).
- [54] P. Zheng, B. D. Ozsdolay, and D. Gall, Epitaxial growth of tungsten layers on MgO(001), *J. Vac. Sci. Technol. A* **33**, 061505 (2015).
- [55] R. Witte, R. Kruk, M. E. Gruner, R. A. Brand, D. Wang, S. Schlabach, A. Beck, V. Provenzano, R. Pentcheva, H. Wende, and H. Hahn, Tailoring magnetic frustration in strained epitaxial FeRh films, *Phys. Rev. B* **93**, 104416 (2016).
- [56] I. Suzuki, T. Koike, M. Itoh, T. Taniyama, and T. Sato, Stability of ferromagnetic state of epitaxially grown ordered FeRh thin films, *J. Appl. Phys.* **105**, 07E501 (2009).
- [57] G. C. Han, J. J. Qiu, Q. J. Yap, P. Luo, T. Kanbe, T. Shige, D. E. Laughlin, and J.-G. Zhu, Suppression of low-temperature ferromagnetic phase in ultrathin FeRh films, *J. Appl. Phys.* **113**, 123909 (2013).
- [58] S. Lounis, M. Benakki, and C. Demangeat, Ferromagnetic stabilization of ordered  $B2$  FeRh thin films, *Phys. Rev. B* **67**, 094432 (2003).
- [59] V. Holý, J. Kuběna, E. Abramof, K. Lischka, A. Pesek, and E. Koppensteiner, X-ray double and triple crystal diffractometry of mosaic structure in heteroepitaxial layers, *J. Appl. Phys.* **74**, 1736 (1993).
- [60] U. Pietsch, V. Holý, and T. Baumbach, *High-Resolution X-Ray Scattering from Thin Films and Multilayers* (Springer Verlag, Berlin, 2004).
- [61] C. Baldasseroni, C. Bordel, C. Antonakos, A. Scholl, K. H. Stone, J. B. Kortright, and F. Hellman, Temperature-driven growth of antiferromagnetic domains in thin-film FeRh, *J. Phys.: Condens. Matter* **27**, 256001 (2015).
- [62] J. A. Arregi, M. Horký, K. Fabianová, R. Tolley, E. E Fullerton, and V. Uhlíř, Magnetization reversal and confinement effects across the metamagnetic phase transition in mesoscale FeRh structures, *J. Phys. D: Appl. Phys.* **51**, 105001 (2018).
- [63] M. R. Fitzsimmons, D. Lederman, M. Cheon, H. Shi, J. Olamit, I. V. Roshchin, and I. K. Schuller, Antiferromagnetic domain size and exchange bias, *Phys. Rev. B* **77**, 224406 (2008).
- [64] U. Aschauer, R. Braddell, S. A. Brechbuhl, P. M. Derlet, and N. A. Spaldin, Strain-induced structural instability in FeRh, *Phys. Rev. B* **94**, 014109 (2016).
- [65] J. Kim, R. Ramesh, and N. Kioussis, Revealing the hidden structural phases of FeRh, *Phys. Rev. B* **94**, 180407(R) (2016).
- [66] N. A. Zarkevich and D. D. Johnson, FeRh ground state and martensitic transformation, *Phys. Rev. B* **97**, 014202 (2018).